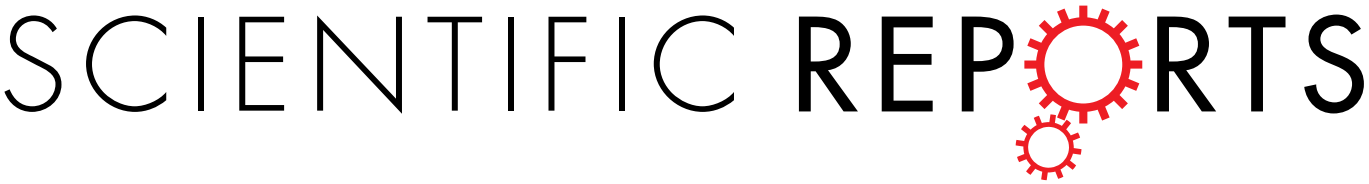

OPEN

Flip-flop Converter of Dual-bistability Using Cavity and Parametric Amplified Four-Wave Mixing

Received: 22 June 2017
Accepted: 23 January 2018
Published online: 06 February 2018

Kangkang Li, Renan Bu, Xiuxiu Wang, Haixia Chen, Dan Zhang, Xinghua Li & Yanpeng Zhang

We study the realization of dual-bistability flip-flop converter in cavity and parametrically amplified four-wave mixing (FWM) process at a four-level cavity atomic system. Using the effect of nonreciprocity optical dual-bistability, we can obtain different output multi-mode states of probe transmission signal and FWM signal. We find the channel equalization ratio and optical contrast between multi-mode states is related to the degree of dual-bistability. Besides, the degree of dual-bistability can be controlled by the input parameters (frequency detuning and powers of the dressing beams). More, using electro-optical modulator and acoustic optical modulator to modulate the powers and frequency detuning, respectively, we can realize the fast conversion between different output states. And the switch speed of this flip-flop converter is about 16 ns. These outcomes may provide foundation for the development of all-optical devices and quantum information processing.

In the last few years, a great deal of optical phenomena based on atomic coherence and quantum interference have attracted intensive attention of many researchers in the multilevel atomic systems. Four-wave mixing (FWM) processes due to atomic coherence have been experimentally reported in all alkali atoms[1–6] and various experimental schemes[7–9]. With widely studied in applications, FWM plays potential roles in the sub shot noise measurements[1,10,11], quantum imaging[12,13], quantum communication[14], slow light[15], storage of light[16] and relative intensity squeezing[5]. Besides, with the self-stabilizing function, FWM can cause the energy transfer of different waves[17–19]. A spontaneous parametric four wave mixing (SP-FWM) process that generates two weak fields can amplify the seeded signal, the phenomenon is called optical parametrically amplification (OPA)[20,21]. More, optical bistability (OB) behavior based on atomic coherence and quantum interference are practiced in recent decades[22,23]. On the other hand, some schemes for realizing optical stability through multi-wave mixing process in an optical cavity have been studied experimentally and theoretically[15], where cavity can provide a feedback as an essential factor for the generation of bistability[24]. OB has also been demonstrated without a cavity using degenerate FWM in atomic vapor with two counter-propagating laser beams[25,26]. The OB in multilevel atoms inside optical cavities[27,28] has been the subject of many recent studies because of its broad application prospects in all-optical logic and memories performance[29,30]. Bistability and instability were also observed in cold clouds of cesium atoms inside an optical cavity, where degenerate Zeeman sublevels participate in the dynamic processes[31].

In this paper, we investigate the nonreciprocity optical dual-bistability (ODB) phenomena of probe transmission signal (PTS) and four-wave mixing (FWM) signal in a composite atom-cavity system both theoretically and experimentally. Based on the relationship of vacuum Ribi splitting and OB[24], the ODB is obtained by scanning the frequency detuning of beams, which is more sensitive than scanning the powers. The nonreciprocity of frequency (frequency offset, in x direction) and intensity (shape change, in y direction) between the two signals (from the rising and falling edges in one frequency scanning round trip) are attributed to "∞"-shape non-overlapping region[32], which can reflect the degree of dual-bistability directly. Besides, the frequency offset is caused by the cavity feedback dressing effect and has been amplified by the effect of vacuum induced enhancement in cavity[24]. Moreover, the nonlinear refractive index and the enhancement and suppression of FWM cavity mode have been studied. By changing the frequency detuning and the powers of dressing beam, the feedback intensity will

Key Laboratory for Physical Electronics and Devices of the Ministry of Education & Shaanxi Key Lab of Information Photonic Technique, Xi'an Jiaotong University, Xi'an, 710049, China. Correspondence and requests for materials should be addressed to Y.Z. (email: ypzhang@mail.xjtu.edu.cn)

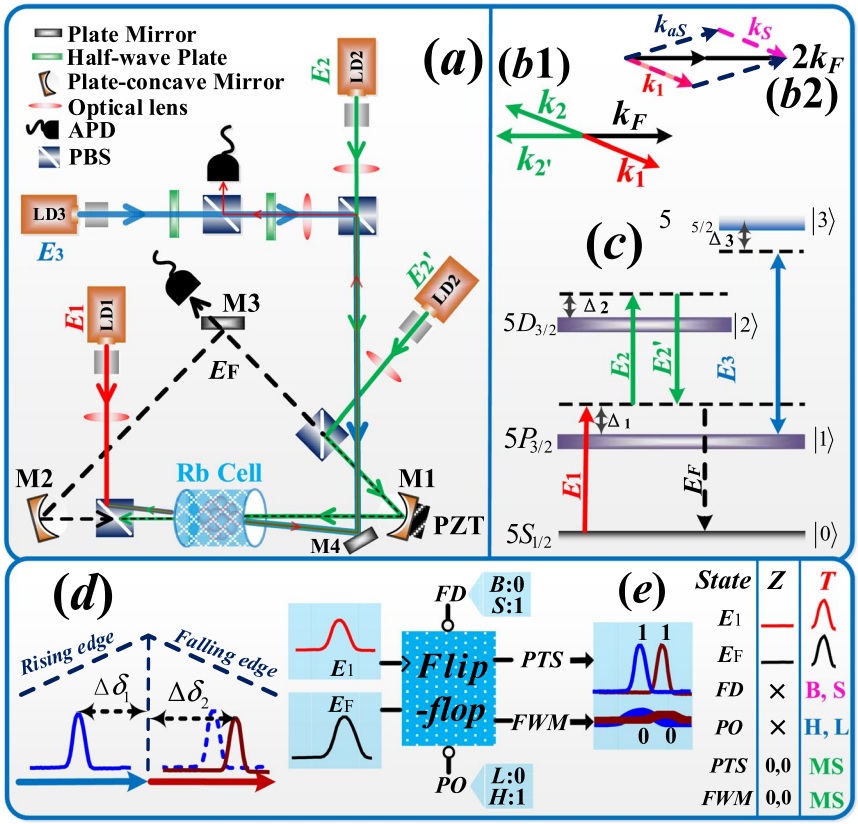

Figure 1. (**a**) Experimental setup. PBS: polarization beam splitter; APD: avalanche photodiode detector; PZT: piezoelectric transducer, which can control the length of cavity; LD: laser device; M1: plate-concave mirror; M2: plate-concave mirror; M3: plate mirror; M4: high reflectivity mirror. (**b1**) Phase-matching geometrical diagram of the cavity-FWM processes; (**b2**) Phase-matching geometrical diagram of the PA-FWM processes. (**c**) Energy-level diagram for the laser coupling configuration in ^{85}Rb vapor. (**d**) The "∞"-shape non-overlapping region between the two signals (from the frequency-rising and frequency-falling edges in one frequency scanning round trip). (**e**) Schematic diagram of dual-bistability flip-flop. FD: frequency detuning; B: big; S: small; PO: power; L: low; H: high; Z: zero; T: trigger; X: arbitrary value; MS: multi-mode states.

be enhanced or suppressed, which results in many kinds of multi-mode output states of signals. The ODB in FWM process provide a solution for generating the multi-mode output states at a time, which means the signals can convey more information. With the controlling of switch between different output states, the action of this phenomena can be realized as a dual-bistability flip-flop converter. These results may have novel and promising development for generation and potentially applicable in all-optical devices and quantum information processing.

Experimental setup and Basic theory

A composite atom-cavity system contains a four-level ^{85}Rb atomic vapor cell in the optical ring cavity. The details of the experimental setup are described in the **Methods** section. The four relevant energy levels are $5S_{1/2}$ (|0>), $5P_{3/2}$ (|1>), $5D_{3/2}$, (|2>), and $5D_{5/2}$, (|3>) as show in Fig. 1(c). In this system, a weak probe beam $\boldsymbol{E}_1$ (frequency ω_1, wave vector $\boldsymbol{k}_1$, Rabi frequency G_1, vertically polarized) couples the transition |0> to |1>, while a strong pumping beam $\boldsymbol{E}_2$ (ω_2, $\boldsymbol{k}_2$, G_2, horizontally polarized) and another pumping beam $\boldsymbol{E}_{2'}$ (ω_2, $\boldsymbol{k}_2$, G_2, vertically polarized) couples upper transition |1> to |2>. Here the detuning $\Delta_i = \Omega_i - \omega_i$ is defined as the difference between the resonant transition frequency Ω_i and the laser frequency ω_i of $\boldsymbol{E}_i$. Besides, $\boldsymbol{E}_1$ counter-propagates with $\boldsymbol{E}_2$, and $\boldsymbol{E}_{2'}$ propagates along the optical axis of the cavity having an angle of 2° with $\boldsymbol{E}_2$ as show in Fig. 1(a). The external-dressing beam $\boldsymbol{E}_3$ (ω_3, $\boldsymbol{k}_3$, G_3) propagates along $\boldsymbol{E}_2$ direction and drives the other upper transition |1> to |3>. When all incident beams are focused at the center of the rubidium cell by optical lenses, a phase conjugate FWM signal $\boldsymbol{E}_F$ (ω_F, $\boldsymbol{k}_F$, G_F, horizontally polarized) is satisfying the phase-matching condition ($\boldsymbol{k}_F = \boldsymbol{k}_1 + \boldsymbol{k}_2 - \boldsymbol{k}_{2'}$ as show in Fig. 1(b1)) and propagates in the opposite direction of $\boldsymbol{E}_2$, which means the signal of $\boldsymbol{E}_F$ is mode-matched to the cavity and can form cavity mode. The cavity transmission spectrum of $\boldsymbol{E}_F$ leaked from M3 is detected by an avalanche photodiode detector (APD). According to the energy system and Liouville pathways, the generated $\boldsymbol{E}_F$ can be obtained by solving the density-matrix equations, the third-order density matrix element as follow:

$$\rho_{10F}^{(3)} = (iG_1)(iG'_2)(iG_2)/(d_1^2 d_2). \tag{1}$$

where $d_1 = \Gamma_{10} + i\Delta_1$, $d_2 = \Gamma_{20} + i(\Delta_1 + \Delta_2)$, $G_i = \mu_{ij}\boldsymbol{E}_i/\hbar$ ($i, j = 1, 2, 2'$) is the Rabi frequency between levels $|i> \rightarrow |j>$, and μ_{ij} is the dipole moment; $\Gamma_{ij} = (\Gamma_i + \Gamma_j)/2$ is the decoherence rate between |i> and |j>. Then, the

generated $\boldsymbol{E}_F$ field can oscillate and circulate inside the three-mirrors ring cavity while $\boldsymbol{E}_1$, $\boldsymbol{E}_2$ and $\boldsymbol{E}_{2'}$ cannot, which is caused by the direction of angle and effect of PBS. Besides, if the atomic transition $|0>\rightarrow|1>$ is resonant with cavity and the atom cavity coupling is strong enough, the atom-cavity coupling needs to be considered in the system. By solving the master equation of the cavity field evolution and the density matrix operators (the details of the solving process are described in the **Methods** section), we can get the cavity mode of $\boldsymbol{E}_F$ by solving master equation as:

$$a_{FWM} = -g\sqrt{N}G_F/[d_4(d_1 + g^2N/d_4 + |G'_2|^2/d_2 + |G_3|^2/d_3]. \quad (2)$$

where $d_3 = \Gamma_{30} + i(\Delta_1 + \Delta_3)$; $d_4 = \gamma + i(\Delta_1 - \Delta_{ac})$; g is the single-atom-cavity coupling strength and N is the atom number; $gN^{1/2}$ represents the atom–cavity coupling which is caused by the combined action between resonant fluorescence of $\boldsymbol{E}_1$ and vacuum induced enhancement of FWM; the term g^2N/d_4 represents the cavity dressing effect; the terms $|G'_2|^2/d_2$ and $|G'_3|^2/d_3$ are the internal-dressing effect of $\boldsymbol{E}_{2'}$ and $\boldsymbol{E}_3$, respectively.

Specifically, by considering FWM process in the atom-cavity system with strong self-Kerr nonlinear effect, there exists an un-neglected cavity feedback effect (also a self-dressing effect)[24]. Clearly, the generated $\boldsymbol{E}_F$ field have a self-dressing effect of $|G_F|^2$, which is derived from the relatively strong feedback effect. This self-dressing effect have similar influence with $\boldsymbol{E}_1$, $\boldsymbol{E}_2$, $\boldsymbol{E}_3$ and g^2N, so Eq. (2) can be rewritten as:

$$a_{FWM} = -g\sqrt{N}G_F/[d_4(d_1 + g^2N/d_4 + |G'_2|^2/d_2 + |G_3|^2/d_3 + |G_F|^2/\Gamma_{00})]. \quad (3)$$

Besides, the probe beam $\boldsymbol{E}_1$ has a sufficiently low power, as well as is far detuned from $|0>\rightarrow|1>$. Moreover, with enhanced cavity mode of $\boldsymbol{E}_F$, a SP-FWM process will occur in the system, which can generate two weak fields (Stokes field $\boldsymbol{Es}$ and anti-Stokes field $\boldsymbol{Eas}$ which satisfying the phase-matching condition $2\boldsymbol{k}_F = \boldsymbol{ks} + \boldsymbol{kas}$). Therefore, the $\boldsymbol{E}_1$ is naturally injected into the input Stokes or anti-Stokes port of the SP-FWM process as shown in Fig. 1(b2), and the injection will serve as an OPA process (with phase-matching conditions $\boldsymbol{k}_{aS} = 2\boldsymbol{k}_F - \boldsymbol{k}_1$ and $\boldsymbol{k}_S = 2\boldsymbol{k}_F - \boldsymbol{k}_1$) assisted by the cascaded nonlinear process. The signal of $\boldsymbol{E}_1$ beam that amplify by OPA-FWM process is named as PTS, and it is detected by the other APD. The photon numbers of the output Stokes and anti-Stokes fields in the amplification process with injection are described in the **Methods** section.

Further, by turning on probe and coupling fields, the first-order density matrix element with consideration of the dressing effects from $\boldsymbol{E}_1$, $\boldsymbol{E}_3$ and $\boldsymbol{E}_F$ is given via Liouville pathways:

$$\rho_{10}^{(1)} = iG_1/(d_1 + G_1^2/\Gamma_{00} + G_3^2/d_3 + |G_F^A|^2/\Gamma_{00}). \quad (4)$$

What's more, similarly to the proposed concept of vacuum induced transparency, the vacuum induced non-reciprocity responses for PTS and FWM are caused by $|G_F|^2$. As this cavity feedback dressing term $|G_F|^2$ is not equal between the signal curves in the frequency-increasing and frequency-decreasing processes (corresponding to the rising and falling edges in one frequency scanning round trip, respectively), the generated nonreciprocity ODB of folded signals could exist "∞"-shape non-overlapping region for scanning the frequency detuning of probe or cavity, which includes the frequency offset in x direction and the shape change in y direction. At first, there exists frequency offset ($\Delta\upsilon$) between the two peaks or dips in the same baseline. Whereas the nonreciprocity can be interpreted by the change of nonlinear refractive index $\Delta n'$, which is given as:

$$\Delta n' = N\left(n_{2up}I_{up} - n_{2down}I_{down}\right) = \Delta\sigma c/\omega_p l. \quad (5)$$

where term $\Delta\sigma = \Delta\upsilon n1l/c$ is the phase delay and $\Delta\upsilon$ is the frequency difference that can reflect the ODB phenomenon directly; I_{up} (I_{down}) is the feedback intensities of the signals for the PTS and FWM on the two side ramps generated at the same frequency scan. n_{2up} (n_{2down}) is the nonlinear refractive index coefficient that can be generally expressed as $n_{2up} \approx n_{2down} \approx n_2 = \mathrm{Re}[\chi^{(3)}/(\varepsilon_0 c n_0)]$, which is the mainly dominated by the Kerr coefficient of $\boldsymbol{E}_2$. The nonlinear susceptibility is:

$$\Delta n' = Nn_2\left(I_{up} - I_{down}\right) = \Delta\sigma c/\omega_p l. \quad (6)$$

Besides, the shape change of the signals can also advocate the ODB effect in the composite cavity-atom system which can be understood through requirement for the dressing suppression and enhancement. When considering the different feedback dressing on the rising and falling edges, the signal will meet different enhancement (or suppression) conditions. For instance, when we scan Δ_3, the primary A-T splitting is caused by $\boldsymbol{E}_3$ whose corresponding eigenvalues are $\lambda_\pm = [\Delta_3 \pm (\Delta_3^2 + 4|G_3|^2)^{1/2}]/2$, so the suppression and enhancement conditions of G_3 are $\Delta_1 + \Delta_3 = 0$ and $\Delta_1 + \lambda_\pm = 0$, respectively. The secondary A-T splitting is caused by the feedback dressing term G_F whose corresponding eigenvalues are $\lambda_{+\pm} = [\Delta_3{}'^2 \pm (\Delta_3{}'^2 + 4|G_F|^2)^{1/2}]/2$ ($\Delta_3{}' = -\Delta_1 - \lambda_+$), and the suppression and enhancement conditions are $\Delta_1 + \Delta'_3 = 0$ and $\Delta_1 + \lambda_\pm + \lambda_{+\pm} = 0$, respectively. Further, when we scan Δ_{ac}, the split energy levels are $\lambda_{+\pm} \pm gN^{1/2}$ and λ_-, where $\lambda_{++\pm} = [\Delta_{ac}{}' \pm (\Delta_{ac}{}' + 4g^2N)^{1/2}]/2$ ($\Delta_{ac}{}' = -\Delta_{ac} - \lambda_{+\pm}$), the respective suppression and enhancement conditions are $\Delta_1 + \Delta_{ac}{}' = 0$ and $\Delta_1 + \lambda_\pm + \lambda_{+\pm} + \lambda_{++\pm} = 0$.

Results and Discussion

In our experiment, we investigate the multi-mode output states that is modulated by the different input parameters. Firstly, we obtain the nonreciprocity of the probe transmission signal (PTS) and the cavity mode four-wave mixing (FWM) signal by scanning the frequency detuning of external-dressing field $\boldsymbol{E}_3$ (Δ_3) or cavity length (namely, Δac). The cavity length is controlled by the PZT (connecting with plate-concave mirror M1) at on left direction is "frequency-rising edge" and at the other direction is "frequency-falling edge" in Fig. 1(a1). That signals come from electromagnetically induced transparency (EIT) window $\Delta_1 + \Delta_2 = 0$. The curves of PTS perform

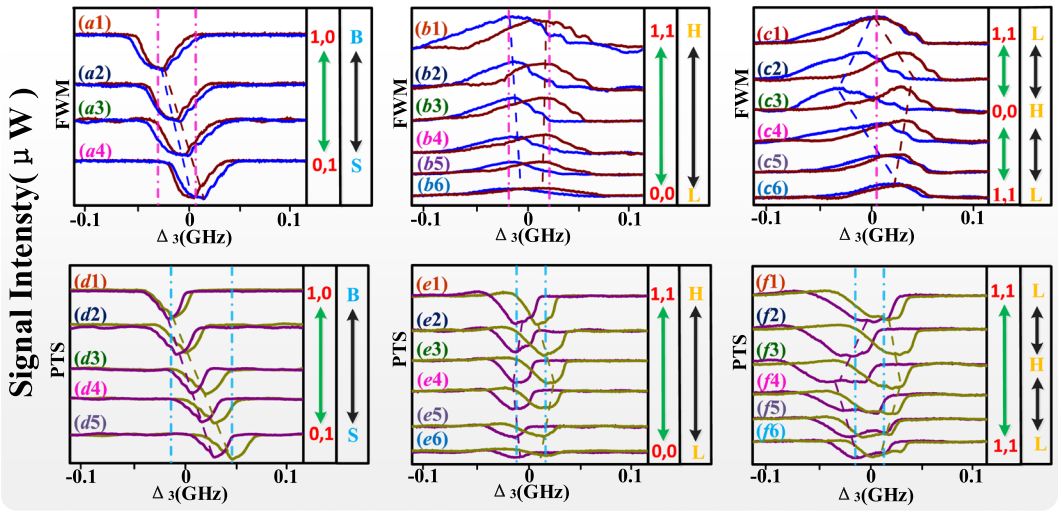

Figure 2. All the experiment curves are "T" (trigger) state; B: big; S: small; L: low; H: high. 0,0: output state of signals; 1,1: output state of signals. 0,1: output state of signals; 1,0: output state of signals. (**a**–**c**) and (**d**–**f**) measured cavity mode (FWM) and PTS, respectively. (**a**,**d**) are obtained against versus Δ_3 at discrete $\Delta 1$ from "B" state to "S" state. (**b**,**e**) are obtained against versus Δ_3 at different points of $\boldsymbol{E}_3$ power from "H" state to "L" state. (**c**,**f**) are obtained against versus Δ_3 at different points of $\boldsymbol{E}_1$ power from "L" state to "H" state then to "L" state.

the combination of electromagnetically induced absorption (EIA) dip and gain peak, which can express as $I_p \propto (I_0 - \mathrm{Im}\rho_{10}^{(1)} + |\rho_{01}^{(3)}|^2)$ (where I_0 is the intensity of the probe field without Doppler absorption; $\rho^{(3)}{}_{01}$ and $\rho^{(1)}{}_{10}$ (in Eq. (6)) show as gain peak and EIA dip, respectively). Meanwhile, the intensity of cavity mode FWM signal is related to a_{FWM} in Eq. (3). In Fig. 1(d), with scanning Δ_3, the left and right curves of the bell shaped represent the frequency-rising edge and frequency-falling edge, respectively, and the vertical curve represents the turning point of the round trip. Correspondingly, there are the signals of F cavity mode FWM, where the left (right) peaks belong to the signals of rising (falling) edge in one frequency scanning round trip. Besides, the frequency detuning between left peak and turning point T is $\Delta\delta_1$, and the frequency detuning between right peak and T is $\Delta\delta_2$. Therefore, when fold the signals on the two edges (rising and falling) from the maxima of the ramp curves point T do not overlap, the frequency offset can express as $\delta = \Delta\delta_2 - \Delta\delta_1$. In our results, we also use this way ($\delta = \Delta\delta_2 - \Delta\delta_1$) to analyze the frequency offset. Besides, it is obvious that the shape of right peak is different from left peak. Therefore, the degree of nonreciprocity can be demonstrated by non-overlapping region includes frequency offset and shape change which can be approximately viewed with infinite sidebands, so we named this kind of nonreciprocity as "∞"-shape ODB.

Secondary, the action of ODB phenomena can be realized as a dual-bistability flip-flop converter and schematic diagram as show in Fig. 1(e), where $\boldsymbol{E}_1$ is trigger signal, $\boldsymbol{E}_F$ is input signal, FD (frequency detuning) and PO (power) are input parameters, PTS and FWM are output multi-mode states. There also have two states ("zero" state and "trigger" state) of this flip-flop and it mainly works at "trigger" state. FD is controlled by an electro-optical modulator and the speed is 10 *ns*, while PO is controlled by an acoustic optical modulator and the speed is 12 *ns*. The switching speed is controlled by the atomic coherence time that is mutable by the phonon effect from microseconds to nanoseconds. The total switching speed (16 *ns*) of this flip-flop converter is taken to be the quadrature sum of several independent contributions. In following experimental results (Figs 2–4), with changed input parameters, we realize the fast conversion between different output multi-mode states by analyzing "∞-shape non-overlapping region and optical contrast of folded signals.

In Fig. 2, we discuss the output multi-mode states of the PTS and cavity mode FWM signal ($\boldsymbol{E}_F$) versus the frequency detuning of $\boldsymbol{E}_3$ (Δ_3). By changing frequency detuning (FD) and power (PO) of dressing fields, we realize the switch action between different output multi-mode states. In Fig. 2(a), the signal of $\boldsymbol{E}_F$ is measured when versus Δ_3 at discrete Δ_1, where the dip of signal curve is lower than the baseline that represents suppression effect of $\boldsymbol{E}_3$. The curves of FWM signal is related to a_{FWM} in Eq. (3). The dip gets the maximum value in Fig. 2(a4) where satisfies window $\Delta_1 + \Delta_2 = 0$ and $\Delta_1 + \Delta_3 = 0$ together, which means the value of Δ_2 is equal to Δ_3. Since the two peaks in Fig. 2(a) have the same baseline, the cavity feedback dressing (also a self-dressing) term $|G_F|^2/\Gamma_{00}$ on the rising and falling edges are not equal in Eq. (3). Hence, the feedback intensity I_{up} is not equal to I_{down} while $n_{2up} \approx n_{2down}$, which can lead to the occurrence of frequency offset ($\Delta\upsilon$) of ODB. From top to bottom, with the increased detuning Δ_1, the $\Delta\upsilon$ appeared larger, which is attributed to increased n_2 in Eq. (6), and the $\Delta\upsilon$ attains maximum value of 6.7 MHz in Fig. 2(a4) where $\Delta 1 = 0$ MHz. In this output state, with H-state of PO, FD is changed from B to S, and the output state of FWM switches from "1,0" to "0,1". Succinctly, the optical contrast for switching application can be defined as $C = (I_1 - I_0)/(I_1 + I_0)$, where I_1 is the intensity of "1"-state and I_0 is the intensity of "0"-state. The optical contrast calculated for this case is 100%. Since, it is obvious from the same baseline that the shape of peaks is different in Fig. 2(a), which is caused by the different suppression conditions. Here we consider second-order splitting caused by $\boldsymbol{E}_3$ and G_F that we have been illustrated theoretically. Because

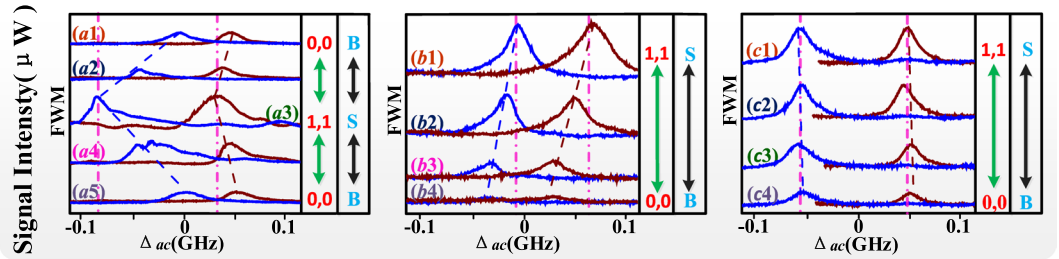

Figure 3. All the experiment curves are "T" (trigger) state by measuring cavity mode (FWM) with beam $\boldsymbol{E}_3$ blocked; B: big; S: small; 0,0: output state of signals; 1,1: output state of signals. In a period, (**a**) versus Δ_{ac} at discrete Δ_1 from "B" state to "S" state then to "B" state; (**b**) versus Δ_{ac} at discrete Δ_1 in a half period (from "S" state to "B" state); (**c**) versus Δ_{ac} at discrete Δ_2 from "S" state to "B" state.

of different G_F on the two edges, the suppression conditions $\Delta_1 + \Delta'_3 = 0$ of two peaks are not same while there are different corresponding eigenvalues λ. And the change of shape difference is minute from top to bottom. While Fig. 2(b,c) are the cavity modes of FWM signals by scanning Δ_3 at different external-dressing field power (P_3) and probe power (P_1), respectively. Comparing with Fig. 2(a), the signals perform gain peak caused by strong enhancement of cavity-dressing effect of $gN^{1/2}$ in Fig. 2(b,c). There frequency offset $\Delta\upsilon$ is also attributed to cavity feedback dressing term $|G_F|^2/\Gamma_{00}$. From bottom to top, with increased P_3, both $\Delta\upsilon$ and shape difference are increasing gradually in Fig. 2(b), which means the power of external-dressing field can alter the state of FWM. Where PO is changed from L to H and the state of FWM switches from "0,0" to "1,1", while the state of FD is B, and the optical contrast calculated for this case is 78%. But in Fig. 2(c), from bottom to top, the change of $\Delta\upsilon$ increases from minimum to maximum in Fig. 2(c4)–(c2), then it becomes minimum again in Fig. 2(c1), it also attributes to changed P_1, which is increased first and then is decreased. In this state, with S-state of FD, PO is changed from L to H and then to L, and the state of FWM switches from "1,1" to "0,0" and then to "1,1" again. The optical contrast calculated for this case is 69%.

In Fig. 2(d–f), there are signals of PTS versus Δ_3 corresponding to Fig. 2(a–c), respectively. The signals are only dip visually, since the suppression is much strong. Same with cavity mode FWM signal, the nonreciprocity ODB of PTS also is induced by cavity feedback dressing term (also parametrically amplified effect) $|G_F|^2/\Gamma_{00}$ in Eqs (3) and (4). In Fig. 2(d), with the Δ_1 increased from top to bottom, the n_2 is increased, the signals in Fig. 2(d5) get the maximum value where Δ_3 around 0 MHz. And the state of PTS also switches from "1,0" to "0,1". In Fig. 2(b,c), all signals satisfy the enhancement condition $\Delta_1 + \lambda_{\pm} + \lambda_{++} = 0$. With the decreasing of P_3 and P_1 in Fig. 2(e1–e6) and Fig. 2(f1–f6), the signal intensity of PTS is increased by the dressing term ${G_3}^2/d_3$ in Eq. (2) and ${G_1}^2/\Gamma_{00}$ in Eq. (6), respectively. Besides, the change process of "∞"-shape non-overlapping region in Fig. 2(e,f) are same with Fig. 2(c). In Fig. 2(e3), the $\Delta\upsilon$ gets maximum value at 31.8 MHz with the largest n_2. For same reason, the $\Delta\upsilon$ gets maximum value at 20.1 MHz in Fig. 2(f3). After that, with the decreasing of P_3 or P_1, the effect of cavity feedback dressing becomes weaken. In these two cases, the states of PTS are switched from "0,0" to "1,1" and "1,1" to "1,1", respectively. And the optical contrasts are more than 90%.

In Fig. 3, with beam $\boldsymbol{E}_3$ blocked, we discuss the output multi-mode states of the cavity mode FWM signal ($\boldsymbol{E}_F$) versus the frequency detuning of cavity (Δ_{ac}). By changing frequency detuning of dressing fields, we realize the switch action between different output multi-mode states. Same with Fig. 2, we recognize the state by analyzing the "∞"-shape non-overlapping region of folded signals.

In Fig. 3(a,b), with beam $\boldsymbol{E}_3$ off, we measured $\boldsymbol{E}_F$ versus Δ_{ac} at discrete $\Delta 1$, where the $\boldsymbol{E}_F$ signal comes from EIT window $\Delta_1 + \Delta_2 = 0$. In Fig. 3(a), we change the detuning Δ_1 in a period but in Fig. 3(b) is just half period. When the detuning Δ_1 is adjusted the position of resonant peaks shifts in the direction of $d\Delta_{ac}/d\Delta_1 = 2/\left[1 - G_4/\left(G_4^2 + 4\left|g\sqrt{N}\right|^2\right)^{1/2}\right]$, and the peak gets the maximum value in Fig. 3(a3). Here we changed the detuning $\Delta 2 = 0$ satisfying the conditions $\Delta_1 - \Delta_{ac} = 0$ and $\Delta_1 - \Delta_2 = 0$, and the window $\Delta_1 - \Delta_{ac} = 0$ comes from dressing effect of $gN^{1/2}$ by the term g^2N/d_4 in Eq. (3). This equation manifests a positive correlation between Δ_{ac} and Δ_1 with a large moving speed satisfying $|d\Delta_{ac}/d\Delta_1| > 2$. Same with Fig. 2, the different feedback dressing parts between I_{up} and I_{down} result in the nonreciprocity of signals. In Fig. 3(a1–a3), the detuning Δ_1 increased first then decreased in Fig. 3(a3–a5). In this case, n_2 is changed from increased to decrease accordingly. The corresponding frequency offset $\Delta\upsilon$ are 49.1 MHz, 113.9 MHz and 47.0 MHz in Fig. 3(a1,a3,a5), respectively. In this state, with L-state of PO, FD of Δ_1 is changed from S state to B state and then to S state again, and the state of FWM switches from "0,0" to "1,1" and then to "0,0" again. The optical contrast calculated for this case is 79%. While in Fig. 3(b), from top to bottom, the decreased detuning Δ_1 result the n_2 to be decreased and corresponding $\Delta\upsilon$ is changed from 66.8 MHz to 53.8 MHz. Where the transition of state is changed from "0,0" to "1,1", and the optical contrast is 96%. All peaks of signals in Fig. 3(a,b) satisfy enhancement condition $\Delta_1 + \lambda_{\pm} + \lambda_{+\pm} + \lambda_{+++} = 0$. In contrast to left peaks, the shape of right peaks is smaller in Fig. 3(a) and is larger in Fig. 3(a), which is attributed to different cavity feedback dressing effect. In Fig. 3(c), Δ_{ac} is scanned at discrete Δ_2 with all beams turned on and setting $\Delta_3 = 0$. When satisfying conditions $\Delta_1 + \Delta_2 = 0$, $\Delta_1 - \Delta_{ac} = 0$ and $\Delta_1 + \Delta_3 = 0$, we can get the maximum value in Fig. 3(c1). From top to bottom, the increased detuning Δ_2 result the decreased n_2, and one can

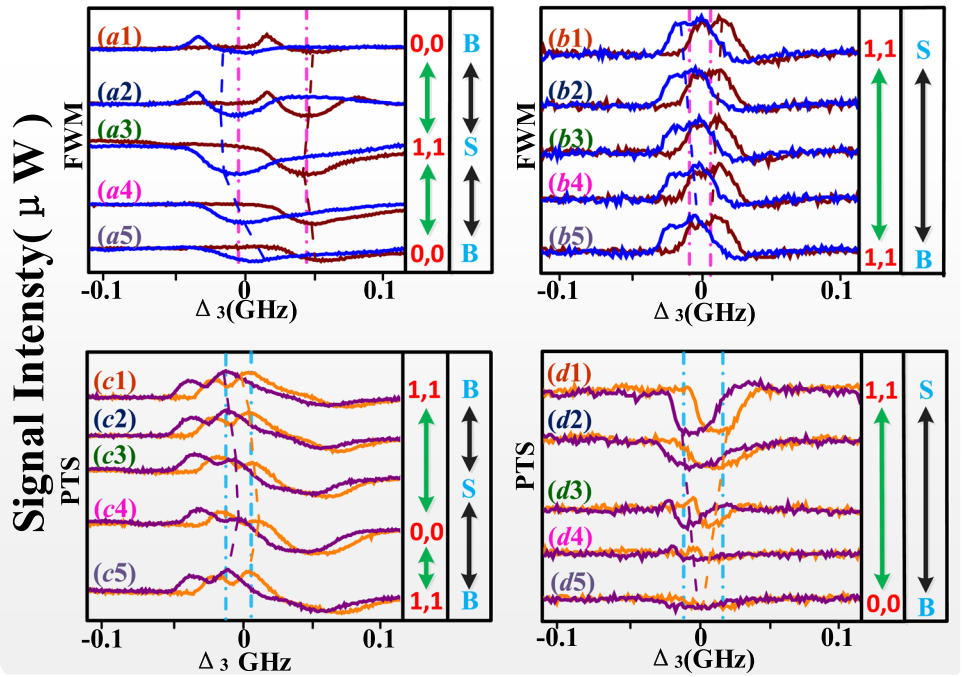

Figure 4. All the experiment curves are "T" (trigger) state by measuring cavity mode (FWM) and PTS; B: big; S: small; 0,0: output state of signals; 1,1: output state of signals. (**a**) and (**c**) are obtained against versus Δ_3 at discrete $\Delta 1$ from B-state to S-state then to B-state. (**b**,**d**) are obtained against versus Δ_3 at discrete Δac from S-state to B-state.

witness that the frequency offset $\Delta\upsilon$ in Fig. 3(c) is approximately 110 MHz. Where the change of ODB phenomena is very small due to saturation effect. Here the transition of state is similar to Fig. 3(b), but the optical contrast is 80%.

Same with Fig. 2, in Fig. 4, we discuss the output multi-mode states of the PTS and cavity mode FWM signal ($\boldsymbol{E}_F$) versus the frequency detuning of $\boldsymbol{E}_3$ (Δ_3). By changing frequency detuning of dressing fields, we realize the switch action between different output multi-mode states. Using the phenomenon of ODB, we investigate this action by analyzing the "∞"-shape non-overlapping region of folded signals. And same with Figs 2 and 3, the nonreciprocity of signals is also caused by different feedback dressing between two edges (rising and falling edges) in Fig. 4.

In Fig. 4(a,b), the curves represent $\boldsymbol{E}_F$ signal by scanning the dressing detuning $\Delta 3$ with the external dressing effect of $\boldsymbol{E}_3$. In Fig. 4(a), when Δ_1 is decreased first in Fig. 4(a1–a3) then is increased in Fig. 4(a3–a5), the measured $\boldsymbol{E}_F$ signal is obtained. Compared to Figs 2(a) and 3(e), the difference is that the signals in Fig. 4(a1,a2) have peaks and satisfy the enhancement condition $\Delta_1 + \lambda_{\pm} + \lambda_{+\pm} = 0$. While the condition of Fig. 4(a3–a5) change from semi-suppression and semi-enhancement to suppression ($\Delta_1 + \Delta_3 = 0$). With the changing of Δ_1, the frequency offset $\Delta\upsilon$ is bit-changed in Fig. 4(a1–a3) and then is decreased from 90.2 MHz to 35.6 MHz gradually. In this state, with L-state of PO, FD of Δ_1 is changed from B-state to S-state and then to B-state again, and the state of FWM switches from "0,0" to "1,1" and then to "0,0" again. The optical contrast calculated in this case is 65%. With increased cavity detuning Δ_{ac} from top to bottom, the signals of $\boldsymbol{E}_F$ as shown in Fig. 4(b). Where the peaks of signals satisfy the enhancement condition $\Delta_1 + \lambda_{\pm} + \lambda_{+\pm} = 0$, the change of degree of nonreciprocity ODB is similar with Fig. 3(b), but the state of FWM is keeping at "1,1" state with H-state of PO.

Figures 4(c,d) are signals of PTS corresponding to Fig. 4(a,b), respectively. In Fig. 4(c), the peaks of signals satisfy the enhancement condition $\Delta_1 + \lambda_{\pm} + \lambda_{+\pm} = 0$. From top to bottom, with changed Δ_1, the enhancement of peaks is weakened first in Fig. 4(c1–c3) then is strengthened in Fig. 4(c3–c5), but the frequency offset $\Delta\upsilon$ is little-changed which is attributed to the enhancement effect. Here the transition of PTS state is contrary to Fig. 4(a). Compared with Fig. 4(c), the signals have dips in Fig. 4(d1,d2) that satisfy the suppression condition $\Delta_1 + \Delta_3 = 0$. Then, the condition of signals change from suppression to semi-suppression and semi-enhancement in Fig. 4(d2–d5). Besides, the degree of "∞"-shape non-overlapping region of ODB phenomena is decreased gradually due to changed suppression and enhancement conditions. Where the transition of state is changed from "0,0" to "1,1", and the optical contrast is 96%.

In the Figs 2–4, the corresponding switching ratio of our flip-flop converter is attributed to the degree of non-overlapping region. If the size of non-overlapping region between dips or peaks in same baseline is big enough, it may be benefit for the division of two states. Such results can be exploited for frequency detuning division multiplexing. Here we use the channel equalization ratio $P = 1 - (\sum_1^{N-1}(S_i - S)^2/S)^{1/2}$ to measure the de-multiplexing effect, where $\boldsymbol{s}$ is the area of one dip or peak, $\boldsymbol{s}_i$ is the area of non-overlapping region. In Fig. 3(a–c), P is near 100%, we shall obtain more balanced and stable spatial channels. In Figs 2(e,f), 3(d–f) and 4(a,c), the channel equalization P can approach 80–90%. We find that the high channel equalization ratio is caused by large of frequency offset $\Delta\upsilon$.

Conclusion

In summary, we study the realization of a dual-bistability flip-flop converter in cavity and PA-FWM. The flip-flop action results from the nonreciprocity ODB phenomena which is induced by self-dressing effect (cavity feedback dressing). The degree of this ODB can reflect by the "∞"-shape non-overlapping region of folded signals, which is changed with different input parameters. Therefore, with high optical contrast and stable spatial channels (channel equalization ratio), we can obtain many kinds of output multi-mode states by controlling the input parameters. By switching the states of PO or FD, we also can realize the convert of output multi-mode states. Specifically, the switch speed of this flip-flop converter is about 16 ns. These results are well explained with theoretical model. The observed phenomenon has novel and promising development for generation and potentially applicable in all-optical devices and quantum information processing.

Methods

Experimental setup. The experiment is performed in a composite atom-cavity system which contains a four-level ^{85}Rb atomic vapor cell in the optical ring cavity as shown in Fig. 1(a). With the length of 38 cm, the cavity is consisted of a plate mirror M3 (with reflectivity of 97.5% at 780 nm) and two plate-concave mirrors (M1 99.9% and M2 97.5% at 780 nm). M1 is mounted on a PZT for adjusting and locking the cavity length. In the setup, a weak probe beam $\boldsymbol{E}_1$ counter-propagates with a strong pumping beam $\boldsymbol{E}_2$. Another pumping beam $\boldsymbol{E}_{2'}$ propagates along the optical axis of the cavity (indicated by the dashed line) having an angle of 2° with $\boldsymbol{E}_2$. Hence a phase conjugate FWM signal $\boldsymbol{E}_F$ propagates in the opposite direction of $\boldsymbol{E}_{2'}$ which means the signal of $\boldsymbol{E}_F$ is mode-matched to the cavity and can form cavity mode. The external-dressing beam $\boldsymbol{E}_3$ propagates at $\boldsymbol{E}_2$ direction. All incident beams are focused at the center of the optical cavity by optical lenses. The temperature of the cell is set to 75 °C in order to have enough atoms in the cavity to enhance the strength of atom-cavity coupling. The cavity transmission spectrum of $\boldsymbol{E}_F$ leaked from M3 (FWM) is detected by avalanche photodiode detector (APD), and the absorption of $\boldsymbol{E}_1$ (PTS) is detected by the other APD.

Evolution of the cavity field and the density matrix operators. Under the weak-cavity field limitation and with all the atoms initially in the ground state $|0\rangle$, the evolution of the cavity field and the density matrix operators obey the following linear equations as:

$$\dot{a} = -[i(\Delta_1 - \Delta_{ac}) + \gamma]a + ig\sqrt{N}\rho_{10} \tag{7}$$

$$\dot{\rho}_{10} = -[i\Delta_1 + \Gamma_{10}]\rho_{10} + iG_F\rho_{00} + ig\sqrt{N}a\rho_{00} + iG_2^*\rho_{20} + iG_3\rho_{30} \tag{8}$$

$$\dot{\rho}_{20} = -[i(\Delta_1 + \Delta_2) + \Gamma_{20}]\rho_{20} + iG_2\rho_{10} \tag{9}$$

$$\dot{\rho}_{30} = -[i(\Delta_1 + \Delta_3) + \Gamma_{30}]\rho_{30} + iG_3^*\rho_{10} \tag{10}$$

where the over-dots represent the first-order derivative with respect to time t; γ is the decay rate for the cavity; $\Delta_{ac} = \omega_{10} - \omega_c$ is the detuning of the cavity field with cavity resonant frequency ω_c, $G_F \propto \sqrt{2/\varepsilon_0 2c\hbar}N\mu^2\rho_{F2}^{(3)}$, $g\sqrt{N}$ results from the resonant florescence induced by $\boldsymbol{E}_1$ and treated as the strength of atom-cavity coupling with single-atom-cavity coupling strength g and atom number N, and the atom-cavity coupling strength has a similar dressing effect with internal-dressing effects of $\boldsymbol{E}_1$, $\boldsymbol{E}_2$, $\boldsymbol{E}_{2'}$ and external-dressing effect of $\boldsymbol{E}_3$.

The photon numbers of the output Stokes and anti-Stokes fields. With the amplification of OPA-FWM process, the photon numbers of the output Stokes and anti-Stokes fields with $\boldsymbol{E}_1$ injection are described as:

$$N_S = \langle \hat{a}_{out}^+ \hat{a}_{out} \rangle = \frac{1}{2}[\cos(2t\sqrt{AB}\sin\frac{\varphi_1 + \varphi_2}{2}) + \cosh(2t\sqrt{AB}\cos\frac{\varphi_1 + \varphi_2}{2})]|\alpha|^2. \tag{11}$$

$$N_{aS} = \left\langle \hat{b}_{out}^+ \hat{b}_{out} \right\rangle = \frac{1}{2}\frac{B}{A}[\cosh(2t\sqrt{AB}\cos\frac{\varphi_1 + \varphi_2}{2}) - \cos(2t\sqrt{AB}\sin\frac{\varphi_1 + \varphi_2}{2})]|\alpha|^2. \tag{12}$$

where $\hat{a}^+(\hat{a})$ and $\hat{b}^+(\hat{b})$ attribute to the Stokes and anti-Stokes fields, respectively; $|\alpha|^2 = \pi\varepsilon_0 c\hbar(G_{AF}r/\mu_{10})^2/2\omega_1$ denotes the intensity of PA-FWM, r is the radius of the probe field, G_{AF} is the PA-FWM amplification factor, and $G_{AF} \propto \sqrt{2/\varepsilon_0 c\hbar}N\mu^2\rho^{(3)}$. The modulus A and B (phase angles φ_1 and φ_2) defined in $\rho_{01(S)}^{(3)} = Ae^{i\varphi_1}$ and $\rho_{01(aS)}^{(3)} = Be^{i\varphi_2}$ for $\boldsymbol{E}_S$ and $\boldsymbol{E}_{aS}$, respectively.

References

1. Slusher, R. E., Hollberg, L. W., Yurke, B., Mertz, J. C. & Valley, J. F. Observation of squeezed states generated by four-wave mixing in an optical cavity. *Phys. Rev. Lett.* **55**, 2409 (1985).
2. Harada, K. L., Mori, K., Okuma, J., Hayashi, N. & Mitsunaga, M. Parametric amplification in an electromagnetically-induced-transparency medium. *Phys. Rev. A* **78**, 013809 (2008).
3. Zlatkovic, B., Krmpot, A. J., Šibalić, N., Radonjic, M. & Jelenkovic, B. M. Efficient parametric non-degenarate four-wave mixing in hot potassium vapor. *Laser Phys. Lett.* **13**, 015205 (2016).
4. Turnbull, M. T., Petrov, P. G., Embrey, C. S., Marino, A. M. & Boyer, V. Role of the Phase-Matching Condition in Non-Degenerate Four-Wave Mixing in Hot Vapors for the Generation of Squeezed States of Light. *Phys. Rev. A* **88**, 033845 (2013).
5. McCormick, C. F., Marino, A. M., Boyer, V. & Lett, P. D. Strong low-frequency quantum correlations from a four-wave-mixing amplifier. *Phys. Rev. A* **78**, 043816 (2008).

6. Guo, M. J. *et al.* Experimental investigation of high-frequency-difference twin beams in hot cesium atoms. *Phys. Rev. A* **89**, 033813 (2014).
7. McCormick, C. F., Boyer, V., Arimondo, E. & Lett, P. D. Strong relative intensity squeezing by four-wave mixing in rubidium vapor. *Opt. Lett.* **32**, 178 (2007).
8. Glassner, D. S. & Knize, R. J. Reduced angular dependence for degenerate four-wave mixing in potassium vapor by including nitrogen buffer gas. *Appl. Phys. Lett.* **66**, 1593 (1995).
9. Lanzerotti, M. Y., Schirmer, R. W. & Gaeta, A. L. High-reflectivity, wide-bandwidth optical phase conjugation via four-wave mixing in potassium vapor. *Appl. Phys. Lett.* **69**, 1199 (1996).
10. Gao, J. R., Cui, F. Y., Xue, C. Y., Xie, C. D. & Kunchi, P. Generation and application of twin beams from an optical parametric oscillator including an α-cut KTP crystal. *Opt. Lett.* **23**, 870 (1998).
11. Pooser, P. C. & Lawrie, B. Ultrasensitive measurement of microcantilever displacement below the shot-noise limit. *Optica.* **2**, 393 (2015).
12. Boyer, V., Marino, A. M., Pooser, R. C. & Lett, P. D. Entangled images from Four-Wave Mixing. *Science.* **321**, 544 (2008).
13. Clark, J. B., Zhou, Z. F., Glorieux, Q., Marino, A. M. & Lett, P. D. Imaging using quantum noise properties of light. *Opt. Express.* **20**, 17050 (2012).
14. Duan, L. M., Lukin, M. D., Cirac, J. I. & Zoller, P. Long-distance quantum communication with atomic ensembles and linear optics. *Nature* **414**, 413 (2001).
15. Boyer, V., McCormick, C. F., Arimondo, E. & Lett, P. D. Ultraslow Propagation of Matched Pulses by Four-Wave Mixing in an Atomic Vapor. *Phys. Rev. Lett.* **99**, 143601 (2007).
16. Camacho, R. M., Vudyasetu, P. K. & Howell, J. C. Four-wave-mixing stopped light in hot atomic rubidium vapour. *Nat. Photonics.* **3**, 103 (2009).
17. Liu, X. M. Theory and experiments for multiple four-wave-mixing processes with multifrequency pumps in optical fibers. *Physical Review A* **77**, 043818 (2008).
18. Liu, X. M. *et al.* Tunable and switchable multi-wavelength erbium-doped fiber laser with highly nonlinear photonic crystal fiber and polarization controllers. *Laser Phys. Lett.* **5**, 904 (2008).
19. Liu, X. M. *et al.* Stable and uniform dual-wavelength erbium-doped fiber Bragg gratings and photonic crystal fiber. *Opt. Express.* **13**, 142 (2005).
20. Chen, H. X. *et al.* Parametrically amplified bright-state polariton of four- and six-wave mixing in an optical ring cavity. *Scientific Reports.* **4**, 03619 (2014).
21. Zheng, H. B. *et al.* Parametric Amplification and cascaded-nonlinearity processes in common atomic system. *Scientific Reports.* **3**, 01885 (2013).
22. Yariv, A. & Pepper, D. M. Amplified reflection, phase conjugation, and oscillation in degenerate four-wave mixing. *Opt. Lett.* **1**, 16–18 (1977).
23. Winful, H. G. & Marburger, J. H. Hysteresis and optical bistability in degenerate fourwave mixing. *Appl Phys Lett.* **36**, 613 (1980).
24. Yuan, J. M. *et al.* Controllable vacuum Rabi splitting and optical bistability of multi-wave-mixing signal inside a ring cavity. *Phys. Rev. A.* **86**, 063820 (2012).
25. Gauthier, D. J., Malcuit, M. S., Gaeta, A. L. & Boyd, R. W. Polarization bistability of counterpropagating laser beams. *Appl. Phys. Lett.* **64**, 1721 (1990).
26. Ackemann, T., Heuer, A., Logvin, Y. A. & Lange, W. Light-shift-induced level crossing and resonatorless optical bistability in sodium vapor. *Phys. Rev. A.* **56**(3), 2321 (1997).
27. Rosenberger, A. T., Orozco, L. A., Kimble, H. J. & Drummond, P. D. Absorptive optical bistability in two-state atoms. *Phys. Rev. A.* **43**, 6284 (1991).
28. Wang, H., Goorskey, D. J. & Xiao, M. Bistability and instability of three-level atoms inside an optical cavity. *Phys. Rev. A.* **65**, 011801 (2001).
29. Soljačić, M., Ibanescu, M., Johnson, S. G., Fink, Y. & Joannopoulos, J. D. Optimal bistable switching in nonlinear photonic crystals. *Phys. Rev. E.* **66**, 055601 (2002).
30. Barclay, P., Srinivasan, K. & Painter, O. Nonlinear response of silicon photonic crystal microresonators excited via an integrated waveguide and fiber taper. *Opt. Express.* **13**, 801 (2005).
31. Lambrecht, A., Giacobino, E. & Courty, J. M. Optical nonlinear dynamics with cold atoms in a cavity. *Opt Commun.* **115**, 199 (1995).
32. Zhang, Z. Y. *et al.* Comparison between optical bistabilities versus power and frequency in a cavity-atom system. *Opt. Express* **25**, 8916 (2017).

Acknowledgements

This work was supported by the National Key R&D program of China (2017YFA0303700), the National Natural Science Foundation of China (No. 11474228, 61605154, 11604256), and the Key Scientific and Technological Innovation Team of Shaanxi Province (No. 2014KCT-10).

Author Contributions

K.K.L. wrote the main manuscript and contributed to experimental work. Y.P.Z. provided the idea. R.A.B., contributed to the presentation and execution of the theoretical work. All authors discussed the results and contributed to the writing of the manuscript.

Additional Information

Competing Interests: The authors declare that they have no competing interests.

Publisher's note: Springer Nature remains neutral with regard to jurisdictional claims in published maps and institutional affiliations.